Published in: Journal of Geophysical Research-Space Physics (2006), vol. 111, iss. A5
Status: Postprint (Author's version)

Global auroral proton precipitation observed by IMAGE-FUV: Noon and midnight brightness dependence on solar wind characteristics and IMF orientation

Valérie Coumans,[1] Jean-Claude Gérard,[1] Benoît Hubert,[1] and Matthieu Meurant[2]

[1]*Laboratoire de Physique Atmosphérique et Planétaire, Université de Liège, Liège, Belgium.*
[2]*Institute for Space Research, University of Calgary, Calgary, Alberta, Canada.*

[1] The brightness of proton aurora observed near solar maximum at summer and winter solstices with the FUV-SI12 global imager on board the IMAGE satellite has been correlated with the solar wind and the interplanetary magnetic field characteristics measured by ACE satellite instruments. By contrast to the electron aurora, we find a strong correlation both on nightside and dayside between the proton precipitated power and the solar wind dynamic pressure calculated with 1 -hour averaged solar wind data. For both southward and northward IMF, the proton power increases with $|B_Z|$, but much more rapidly on the nightside for southward IMF orientation. Correlations for the nightside aurora were also calculated with a series of solar wind-magnetosphere coupling functions. We find highest correlation coefficients for expressions containing the dynamic pressure or involving the solar wind electric field in the Y-Z plane. The influence of the solar wind dynamic pressure on the proton aurora is tentatively explained by the effect of the pressure on the shape of the magnetosphere, generating stretching of the magnetotail and proton precipitation but also by other coupling processes between the solar wind and the magnetosphere. Adding FUV-WIC and SI13 electron aurora images in the study, we determine how proton and electron precipitations simultaneously react to solar wind and IMF characteristics and Kp. Results shows that protons are more reactive to dynamic pressure variations than electrons when B_z is positive, while the influence on of both types of particles is similar for negative B_z. The precipitating proton flux is found proportionally larger compared with the electron flux when the total auroral flux increases for low activity level. Instead, for high activity level, the proportion of the proton and the electron powers are similar when auroral power increases. Consequently, it is suggested that similar mechanisms cause proton and electron auroral precipitation for high activity levels, while they appear somewhat decoupled for lower activity conditions.

1. Introduction

[2] Variations in the solar wind have an important influence on the magnetosphere and on the characteristics of the aurora. It is well known that abrupt solar wind variations such as pressure pulses associated with CMEs can induce significant auroral precipitation [*Zhou and Tsurutani,* 1999; *Chua et al.,* 2001; *Hubert et al.,* 2003; *Meurant et al.,* 2003b]. The morphology of the aurora has also been extensively studied as a function of the IMF orientation. For example, *Lansen and Danielsen* [1978] studied quiet time arcs observed from the Greenland all-sky camera network. They showed that the oval arc pattern is prominent for southward IMF, and practically vanished as steady IMF is shifted toward a northward direction. They also showed a contraction of the oval pattern depending the sign of B_y: for positive B_y, the contraction takes place in essentially the evening sector of the oval, while for negative B_y, the morning sector is more affected. The location of the electron auroral oval had also been studied in different MLT sectors in relation with the IMF and the solar wind characteristics. *Kamide and Winningham* [1977] made a statistical study of the "instantaneous" nightside auroral oval, using measurements from the ISIS 1 and 2 satellites. They showed that the north-south component of the IMF plays a dominant role in controlling the motion of the equatorward boundary of the nightside oval. *Makita et al.* [1983] studied the shift of the auroral electron boundaries in the dawn-dusk sector in association with the IMF, from measurements of DMSP-F2 satellite. They showed that the locations of the poleward and the equatorward boundaries are both controlled by the B_z orientation. The dayside aurora is also influenced by changes in the solar wind as shown by *Jacobsen et al.* [1995]. Using ground-based observations, they found that the prenoon aurorae morphology is dependent on the IMF B_z and the solar wind density.

[3] The brightness of the aurora and its control by the solar wind parameters and the IMF have been investigated by *Liou et al.* [1998], using global UVI images from Polar and the solar wind measurements from the Wind satellite. They showed that the afternoon aurora is more active for large IMF cone angle and large solar wind

electric field. The nightside auroral brightness is moderately correlated with the orientation of the B_z components of the IMF and the solar wind velocity, while no effects are induced on the nightside aurora by the solar wind dynamic pressure. They explained the dayside results by a partial penetration of the IMF into the dayside closed magnetic field and the solar wind electric field entering into the magnetosphere via field line reconnections in different locations. The nightside processes controlling the aurora are due to reconnection and viscous-like interactions mechanisms. Using similar data, *Shue et al.* [2002] examined the relationship between auroral brightness and solar wind and IMF characteristics, on the basis of the IMF B_z orientation and the season. They found that both winter and summer precipitation powers are mostly controlled by solar wind density and velocity for southward IMF on the nightside. Globally, these studies indicate that the electron aurora morphology and brightness are strongly influenced by the IMF orientation but also by the solar wind conditions.

[4] The transfer of energy from the solar wind to the magnetosphere, which is the ultimate source of the nightside auroral precipitation, has been the object of extensive studies. *Arnoldy* [1971] used the north-south component of the IMF as a signature in the interplanetary medium for substorms. *Gonzales and Mozer* [1974] suggested that the energy transfer through the reconnection depends on the magneto spheric electric field in the transverse plane. *Akasofu* [1981] suggested a first approximation expression for the solar wind-magneto sphere energy coupling function ε. This expression, already described by *Perreault and Akasofu* [1978], correlates well with the total energy consumption rate of the magnetosphere. They showed that ε is the primary factor controlling the time development of the magnetospheric substorms and storms. This expression indicates that the solar wind and the magnetosphere work together as a dynamo, by which the solar wind couples its energy with the magnetosphere. Other empirical functions were suggested to describe the strength of the solar wind-magnetosphere coupling. *Vasyliunas et al.* [1982] searched for a functional dependence on solar wind parameters of the rate of energy transfer from dimensional analysis constraints. They found that the energy transfer depends on the solar wind dynamic pressure, velocity, and transverse IMF orientation. *Wygant et al.* [1983] used S3-3 measurements of the polar cross polar cap electric potential and compared them with the reconnection electric fields predicted by several theoretical and experimental models. They found best agreement for a dependence on θ_c, the angle between the transverse component of the IMF and the Earth's magnetic field at the magnetopause, with a fourth power of sin θ_c. Other factors influencing the reconnection efficiency are the solar wind velocity and the absolute value of the transverse component of the IMF. *Liou et al.* [1998] made a correlative study of the auroral power derived from Polar UVI observations with the concurrent solar wind and IMF observations from the Wind satellite. Their conclusion was that the response function for nightside aurora is best represented by $VB_t \sin^4(\theta_c/2)$ or $P^{1/6}VB_t \sin^4(\theta_c/2)$ transfer functions.

[5] Processes leading to the proton aurora are much less known than for electron precipitation. *Mende et al.* [2002] listed four processes identified as the cause of the proton precipitation. First, proton aurora can be produced by precipitation from an isotropic proton population injected into a region of closed field lines, for example by dayside reconnection or nightside substorm processes. Second, under some active circumstances, significant precipitation from a stably trapped population can also be produced by pitch angle diffusion due to particle interactions with electric fields (dc or wave). The loss cone is then populated, and particles that were previously trapped then precipitate. Third, precipitation can also be produced when a magnetic reconfiguration compresses the region occupied by protons, for example, following an abrupt solar wind-induced compression of the magnetosphere. Finally, proton precipitation also occurs when particles are scattered in a stretched field line configuration, such that the proton motion violates the adiabatic invariants.

[6] Morphological and quantitative characteristics of the proton aurora have been the subject of several studies, based on ground-based or in situ measurements, but never on global observations as no global imager of proton aurora was available before FUV-SI12. *Hardy et al.* [1989] employed in situ data obtained from ~27,000 polar passes by DMSP spacecraft to build statistical maps of the mean particle energy, number flux, and energy flux that were provided for protons for seven different magnetic activity levels measured by the Kp index. They emphasized the fact that a minimum in the ion energy flux occurs in the prenoon sector, while the maximum value is observed pre-midnight at all levels of activity. *Coumans et al.* [2004b] used IMAGE-FUV observations to map the auroral electron and proton energy fluxes during the summer and winter solstices of year 2000 and to construct a statistical view of the global auroral proton precipitation. They confirmed the "C-shaped" distribution of the proton precipitation with a minimum located in the morning sector, already described by *Hardy et al.* [1989]. They also found that the latitudinal width of the proton oval is larger in summer than in winter so that the globally precipitated proton power is 1.5 times higher in summer than in winter. Moreover, the occurrence probability of intense proton aurora (with energy flux >0.5 mW m^{-2}) was also shown to be nearly three times as high in summer as in winter. By contrast, *Newell et al.* [2005] investigated the seasonality of the ion aurora using one solar cycle of DMSP satellite particle data. One of the results of their study was that the ion aurora is approximately equal in the summer and winter hemispheres in the dusk-midnight sector, while in the sectors

from midnight to dawn, the ion precipitating energy flux is higher in winter than in summer.

[7] Using the set of IMAGE-FUV instruments, *Frey et al.* [2002] studied the signature of the proton aurora in the cusp and its control by the solar wind magnetic field and plasma parameters. They showed that a cusp signature separated from the auroral oval appears in the Lyman-α images only when the IMF has a northward B_z component, but the intensity of the precipitation is not controlled by the magnitude of B_z. Strong correlations between the UV intensity and the dynamic pressure were found, likewise between the location in local time and the IMF B_y component. However, this study concentrated on a localized and specific proton auroral precipitation, characterized by the direct connection between the ionosphere and the interplanetary medium through magnetic reconnection at the high-latitude magnetopause.

[8] The purpose of this study is to determine how the global proton aurora is influenced by variations in the solar wind and to analyze possible correlations between the auroral proton precipitation power and the characteristics of the solar wind and the IMF orientation. We use observations of proton aurora from IMAGE-SI12 and measurements of the solar wind parameters from the ACE satellite. Section 2 explains how the data from both satellites were selected and processed for correlation studies. The solar wind measurements were averaged over the preceding hour, considering the solar wind-magneto sphere coupling as a loading-unloading system. The choice of the time averaging is explained in section 2. Section 3 describes results of correlation between the precipitating proton flux and the solar wind characteristics. Since both proton and electron aurora are observed simultaneously, we analyze the simultaneous behavior of both types of precipitation with variations in the solar wind and present results in section 4. Section 5 discusses the results and suggests how the response of proton aurora to changing activity levels may be understood. Finally, section 6 summarizes the results and the discussion.

2. Data Analysis

2.1. Precipitating Proton Power

[9] The IMAGE satellite has an eccentric orbit with a ~7 Earth radii apogee and a 1000-km perigee. The IMAGE FUV imaging system includes three instruments which provide snapshots of the global northern auroral region every 2 min. The Wideband Imaging Camera (WIC) is mostly sensitive to the LBH bands of molecular nitrogen and the 149.3 nm NI line. The SI12 Spectrographic Imager images the Doppler-shifted Lyman-α emission (121.8 nm) produced by auroral protons, while the SI13 camera isolates the OI 135.6 nm emission [*Mende et al.,* 2000] with some contributions from the N_2 LBH bands. The WIC and SI13 images are contaminated by dayglow on the dayside, which is subtracted using the method described by *Hubert et al.* [2002]. The SI12 images also contain a weak background contribution that is also removed from each individual image. This background signal is mainly due to the geo-coronal H Lyman-α emission at 121.56 nm and depends on the illumination and view angles. A very small contribution also originates from the N 120 nm emission and from some weak N_2 LBH emission lines. Moreover, dark counts in the detector are also present in the SI12 images. This background contribution is small and may be efficiently removed by a mathematical method, consisting of a polynomial least squares fit [*Hubert et al.,* 2002]. The fit is applied to each SI12 image over the region void of auroral emission and the function so determined is then subtracted over the full-observed disk.

Table 1. *Kp Distribution of Data (Used in This Study) of Summer 2000 and Winter 2000-2001 Observations*

Kp	**0**	**1**	**2**	**3**	**4**	**5**	**6**
Summer	374	4443	4529	3559	1769	937	267
Winter	1265	5623	3976	2734	628	0	80
Total	1639	10066	8505	6293	2397	937	347

[10] For each northern hemisphere observations with IMAGE-FUV, the electron energy and energy flux can be calculated from WIC and SI13 images. The proton energy flux can be evaluated from SI12 depending on an assumption on the proton energy, which cannot be determined from the observations. In this study the proton energy is taken from *Hardy et al.*'s [1989] empirical model. The method used to calculate the particle energy flux and associated uncertainties were fully described by *Hubert et al.* [2002], *Meurant et al.* [2003a], and *Coumans et al.* [2004a]. It is based on FUV instrument efficiency function, evaluated from transport and energy degradation models of particles in the Earth atmosphere [*Solomon et al.,* 1988; *Gérard et al,* 2000]. The proton

energy fluxes are obtained from the SI12 count rate using the relationship between the SI12 signal and NOAA in situ measurements of proton precipitation fluxes [*Coumans et al.,* 2002].

[11] This work is a statistical study extending the morphology and seasonal variation study of global auroral proton precipitation by *Coumans et al.* [2004b]. The statistical proton energy flux is studied in connection with the solar wind characteristics and the IMF orientation. The time period of the study is extended over summer 1 June to 10 July 2000 and winter 3 December 2000 to 8 January 2001, which time periods are very close to the solar activity maximum. This corresponds to a total of 30,184 FUV snapshots, including 15,878 summer cases and 14,306 winter cases. The two selected time intervals correspond to very similar values of the mean solar flux, so that the study is not biased by the level of solar activity. The mean $F_{10.7}$ index was 178 in the summer interval and 171 during the winter interval. Table 1 shows the distribution of the number of cases sorted by Kp value. The corresponding mean Kp index was 2.4 in summer, compared with 1.7 in the winter. The difference is not important and, as it is shown hereinafter, does not have a major influence on the seasonality. The power associated with each FUV image is actually dependent on the previous observations because of the integrated time response of the magnetosphere in relation with the solar wind. Therefore the statistical analysis is not based on 30,184 independent data point. This suggests that the individual images should be in some way time-averaged. In our treatment, this time averaging is replaced by binning the auroral powers into intervals of hourly averaged solar wind characteristics values. Since one hour of observations corresponds to ~30 FUV snapshots, the statistics in this work are thus based on about 1000 independent hourly averaged samples.

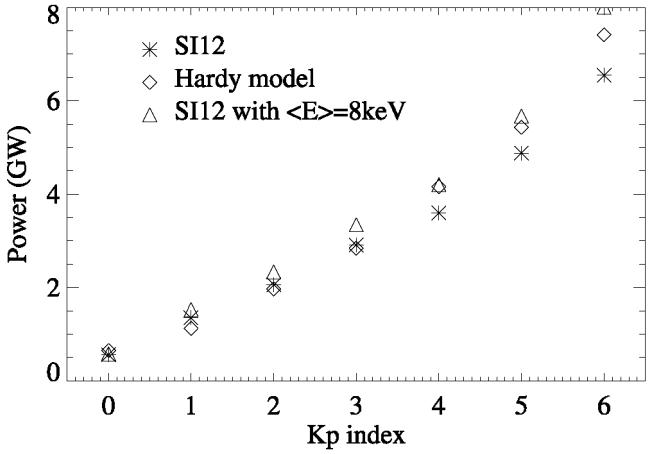

Figure 1*. The averaged proton auroral power from SI12 (stars) and evaluated from the Hardy et al. [1991] proton flux model (diamonds) as a function of the Kp index. The power was calculated between 60° and 80° MLAT over all MLT sectors. The proton power was also deduced from SI12 observations using a fixed averaged energy (8 keV) whatever the geographic location of the precipitation (triangles).*

[12] Using the data base built for this present work, a comparison between the averaged proton auroral power from SI12, evaluated from the 30,184 FUV snapshots, and the one evaluated from the *Hardy et al.* [1991] model of proton flux and energy is presented in Figure 1. The power was calculated between 60° and 80° MLAT over all MLT sectors. Moreover, to test the importance of the assumption on the proton energy, the proton power was also deduced from SI12 observations using a fixed averaged mean energy (8 keV) for all geographic locations. The results are plotted in Figure 1 with triangle symbols. The agreement between the power derived from SI12 and from the empirical model is, at worst, within 20% for Kp = 1. It is within 5% for Kp = 2 or 3 and 10% for higher Kp. The agreement assuming a fixed proton energy is within 15% except for Kp = 0 where it is ~2% and for Kp $\geq$ 6 where it is ~22%. Remembering that the empirical model was built over 9 years of data while we use observations near the solar activity maximum, and all other sources of uncertainties, as discussed by *Coumans et al.* [2004b], we consider the agreement as very satisfactory. It demonstrates the validity of the methodology applied to derive proton fluxes from the SI12 count rate. The global calibration of the method uses the relationship between the SI12 signal and NOAA in situ measurements of proton precipitation from *Coumans et al.* [2002]. Moreover, changing the assumption over the proton energy induces a mean difference of 15%, that is, the same order of magnitude as the model uncertainties.

[13] The study by *Coumans et al.* [2004b] was based on observations covering a period of 12 days in summer 2000 and 15 days in winter 2000. This database included 10,602 FUV snapshots. This study, in contrast to in situ satellite measurements, gives a global picture of the aurora and is equivalent to many orbits of in situ satellite data. In the present study, the database was extended over 40 days in summer 2000 (1 June to 10 July) and 37 days in winter 2000-2001 (3 December to 8 January), corresponding to a total of 30,184 FUV snapshots. As a first step, we verified the seasonal variation of the proton precipitation using IMAGE-FUV observations in summer 2001 and winter 2001-2002. We used 39,129 FUV snapshots, with 20,004 over the period between 1 June and 12 July 2001 and 19,125 between 1 December 2001 and 9 January 2002, respectively. This new database is totally independent of that used in our previous work and, in the way the data were used, FUV snapshots are considered as independent from one another. The averaged Kp index over the summer period is 1.79, while it is 1.77 over the winter period. The averaged Kp index over the full observation period is 1.78, indicating that the magnetic activity in both periods was very similar. Panels in Figure 2 show maps of the winter and the summer averaged proton precipitating fluxes. Figures 2a and 2b are the statistical precipitating flux over summer 2000 and winter 2000-2001, which is the sample of the present work. Figures 2c and 2d show results for the summer 2001 and winter 2001-2002 seasons. A seasonal difference is seen in both panels. The averaged proton oval is wider in latitude in summer than in winter. The flux maximum around 0100 MLT is also higher in summer than in winter, reaching 0.27 mW m^{-2} and 0.30 mW m^{-2} in summer 2000 and 2001, respectively, compared with 0.23 mW m^{-2} and 0.22 mW m^{-2} in winter 2000-2001 and 2001-2002, respectively. Unlike *Newell et al.* [2005], the IMAGE data show a peak in energy flux in the postmidnight sector in summer, rather than in winter. The precipitated proton power integrated between 60° and 80° MLAT over the entire oval still shows seasonal differences, reaching 2.6 GW and 3.0 GW in summer 2000 and 2001, respectively, and 1.4 GW and 1.3 GW in winter 2000-2001 and 2001-2002, respectively. Therefore the summer averaged power is 1.9 and 2.3 times as high as the winter one, respectively. These results thus confirm our previous study based on a smaller database over the year 2000.

[14] We also analyze our database to characterize the proportion of proton energy flux in the region of the cusp compared with the entire oval. The cusp is not apparent on the averaged energy flux map (Figure 2). As it will be discussed more extensively in section 5, the relatively low energy of proton cusp precipitation causes the cusp to be observable by SI12 only under specific conditions. The *Hardy et al.* [1989] spectrograms of the averaged integral number flux shows that the cusp region is located in a sector around noon, 1 to 2 MLT hours wide, and varying in latitude with the Kp index. The cusp is centered on ~80° MLAT for Kp = 0 and ~72° for Kp = 5. However, because of the low energy of precipitating protons in the cusp, the spectrograms of the proton integral energy flux do not show any dayside cusp signature. From the *Hardy et al.* [1989] maps of the average integral number flux, we defined an averaged region for the cusp (between 72° and 82° MLAT and between 1115 and 1245 MLT), and calculated from our data base the fraction ratio of the energy flux in this region relative to the entire oval. We find that the proton energy flux in this sector represents ~1.3% of the entire oval. However, the cusp is not always detected by SI12 because of the low proton average energy.

2.2. Solar Wind Data

[15] The IMF and solar wind measurements from the Advanced Composition Explorer (ACE) satellite have been used to investigate the solar wind control of the proton auroral precipitation. ACE orbits the L1 libration point about 1.5 million km from Earth and 148.5 million km from the Sun. The propagation time of the solar wind between the ACE satellite and the Earth was taken into consideration using the ACE-Earth distance and the measured bulk velocity. The time of the solar wind characteristics measured by ACE was delayed by adding the propagation time evaluated from the solar wind speed measurement. Each FUV image was thus related to the characteristics of the solar wind reaching the magnetosphere when the image was taken. The solar wind-magneto sphere system may be viewed as a loading-unloading system. The magnetosphere has a memory of past events and reacts according to this background history as suggested by *Liou et al.* [1998]. We compared the correlation coefficient between the auroral power and B_z, using various delay time: instantaneous characteristics (averaged over 1 minute), delayed by 5, 10, 20, 30, 45, 60, or 90 min, and averaged over 60 or 90 min before the FUV observations. For the electron aurora, the correlation coefficient between the power and $B_z > 0$ was -0.10, -0.23, and -0.17, respectively, for instantaneous B_z values, for 60 min time-lag, and for 60 min averaged, while the values are -0.28, -0.35, and -0.37 for correlation with $B_z < 0$. A negative correlation coefficient implies a negative slope of the linear regression. For protons, the values of the correlation coefficient are 0.24, 0.20, and 0.15 for $B_z > 0$ and -0.41, -0.43, and -0.43 for $B_z < 0$, respectively, for the same time delay. These results indicate that using solar wind data with a time lag of 60 min or averaging over 60 min present similar correlations. Therefore we present only correlation studies on solar wind and IMF characteristics averaged over 60 min prior to each observation, with the appropriate time shifting for solar wind propagation between the ACE satellite and the Earth. This point will be discussed further in section 3.

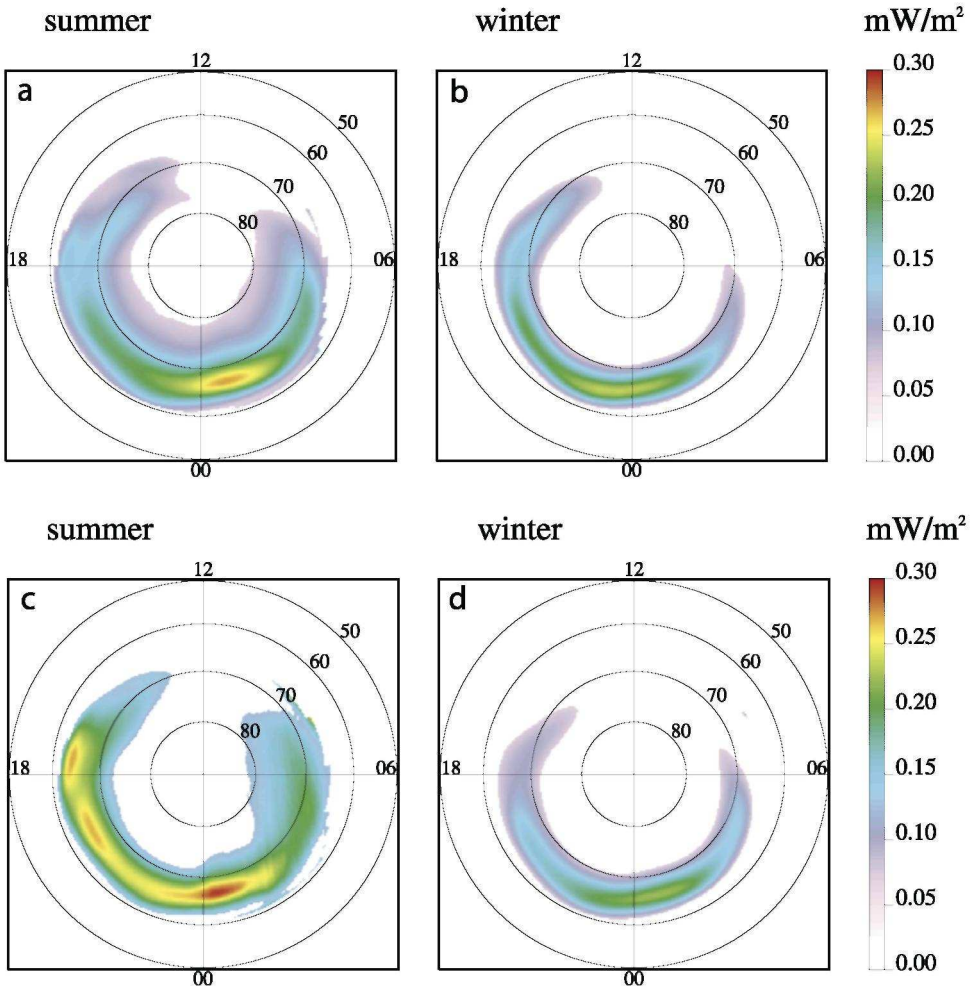

Figure 2. *Maps of the (a and c) winter and the (b and d) summer averaged proton precipitating flux. In Figures 2a and 2b the statistical precipitating flux was calculated with data from the summer 2000 and winter 2000-2001 solstices, corresponding to 30,184 IMAGE-FUV snapshots. In Figures 2c and 2d, 39,129 IMAGE-FUV snapshots around summer 2001 and winter 2001-2002 seasons solstices were used.*

[16] Intercorrelation between solar wind and the IMF characteristics may affect the correlation between the auroral power and these parameters and influence the interpretation of the results. Table 2 shows the cross-correlation matrix between the 3 components of the IMF and the solar wind velocity, density and dynamic pressure for the time period of our sample. The coefficients were calculated for $B_z > 0$ (below the main diagonal in Table 2) and $B_z < 0$ (above the main diagonal in Table 2) separately. A total of 15,322 cases correspond to positive B_z and 14,862 to negative B_z. The density and the dynamic pressure appear as highly correlated, with $r = 0.78$ for $B_z < 0$ and 0.84 for $B_z > 0$, respectively. This result is not unexpected since the dynamic pressure depends linearly on the solar wind density. The transverse IMF components, B_x and B_y, are correlated at ~50% ($r = -0.50$ for $B_z < 0$ and $r = -0.43$ for $B_z > 0$). This result is the signature of the solar wind "garden hose" configuration. The density is also moderately correlated ($r = 0.48$) with $B_z > 0$, but weakly correlated with $B_z < 0$ ($r = 0.21$). A weak negative correlation is obtained between the solar wind velocity and its density ($r = -0.28/-0.32$ for $B_z < 0/B_z > 0$). The correlation between B_x and B_z for southward condition and between B_y and the velocity for northward condition are not significantly different of zero. Except between B_x and B_y, between positive B_z and the density, and between the velocity and the dynamic pressure, the correlations between the IMF and the solar wind characteristics are weak and should not affect the correlation with the auroral power. Finally, the averaged Kp index was evaluated for both signs of B_z. For positive B_z, the averaged Kp is 1.9 and 2.2 for negative B_z. This indicates that there is a small difference in the magnetic activity for the two north-south orientations of the IMF. This is expected since a southward IMF orientation is itself frequently associated with enhanced substorm activity.

Table 2. *Intercorrelation Coefficients of the Solar Wind and IMF Characteristics for Bz > 0 (15,322 Cases, Below the Principal Diagonal) and for Bz < 0 (14,862 Cases, Above the Principal Diagonal)*

	B_x	**B_y**	**B_z**	**V**	**N**	**P dyn**
B_x	.	-0.495 ± 0.006	-0.001 ± 0.008	-0.048 ± 0.008	0.138 ± 0.008	0.141 ± 0.008
By	-0.427 ± 0.007	.	-0.032 ± 0.008	-0.086 ± 0.008	-0.045 ± 0.008	-0.089 ± 0.008
B_z	0.068 ± 0.008	0.026 ± 0.008	.	-0.045 ± 0.008	-0.212 ± 0.008	-0.210 ± 0.008
V	-0.035 ± 0.008	-0.018 ± 0.008	-0.129 ± 0.008	.	-0.285 ± 0.007	0.251 ± 0.008
N	0.179 ±0.008	-0.107 ±0.008	0.481 ± 0.006	-0.321 ± 0.007	.	0.780 ± 0.003
P dyn	0.188 ±0.008	-0.098 ± 0.008	0.367 ± 0.008	0.128 ± 0.008	0.838 ± 0.002	.

3. Control of Proton Precipitation By the Solar Wind and IMF

[17] The dependence of the proton auroral power, calculated from IMAGE-SI12 observations, with the solar wind characteristics and the IMF components is now analyzed. Figures 3 and 4 summarize the proton power versus the IMF and the solar wind characteristics for the 2200-0200 MLT nightside sector and the 1000-1400 MLT dayside sector, respectively. The power data were binned by the three components of the IMF, solar wind density, speed, and dynamic pressure, and averaged. Bins for the B components are 2 nT wide between -8 nT and +8 nT, and the extreme ones include all data points for $B_z < -8$ nT and $B_z > 8$ nT. The solar wind density bins are 2 cm^{-3} between 0 and 16 cm^{-3}, the velocity bins are 50 km s^{-1} between 350 and 700 km s^{-1} , and the dynamic pressure bins range between 0 and 8 nPa in 1 nPa bins. The vertical error bars show one standard deviation of the proton precipitation power associated with the averaged value in each bin. Figure 3 shows that on the nightside, the power is independent of B_x between -5 and 5 nT. For B_x less than -5 nT, it is difficult to discriminate between the scatter of the data and a low and nonlinear increase of the power with B_x intensity. Finally the power increases with positive values of the X component of the IMF higher than 5 nT. A quasi-similar behavior is observed for B_y. The power does not vary with B_y between -7 and 7 nT, while it increases for extreme values. The nightside proton power positively responds to an increase of the B_z magnitude but much more rapidly for southward IMF than for northward IMF. The minimum is for B_z between 0 and 2 nT, where the statistical power reaches 0.50 GW. For southward IMF, it reaches a maximum of 1.37 GW, while for northward IMF the maximum is 0.73 GW. The power shows a moderate increase with the solar wind density. The maximum power is in the density range between 12 and 14 cm^{-3} and reaches twice the minimum value. The solar wind velocity does not appear to control the proton power, while a dynamic pressure increase produces a nearly linear increase of the power. The slope of the regression is 0.15 GW/nPa or 150×10^{15} W/Pa. The plot for the dynamic pressure is not a mix of the density and the velocity curves, even though the dynamic pressure is NV^2. The product of the two quantities is calculated for each individual case, before binning in dynamic pressure range. On the dayside, the trends are globally similar to the nightside. Figure 4 shows that the power is only controlled by extreme values of B_x and B_y. The dayside proton power increases slightly with the solar wind density, while the velocity does not exert any real influence. The major difference with nightside is for B_z. The power increases for both positive and negative B_z values. The trend is more symmetric about $B_z = 0$, so that the regression slopes for $B_z > 0$ and for $B_z < 0$ are both 0.01 GW/ nT. Moreover, the power increases quasilinearly with the dynamic pressure but shows a more moderate dependence (0.054 GW/nPa or 54 x 10^{15} W/Pa) than on the nightside.

[18] Because of the quasilinearity between the proton power and the dynamic pressure or B_z observed in Figures 3 and 4, the correlation coefficients were calculated. They were calculated over the full sample of data (not binned) for both seasons, i.e., over a 30,184 sample data set. The correlation coefficients are summarized in Table 3. These were obtained separately for nightside, between 2200 and 0200 MLT, and dayside, between 1000 and 1400 MLT, with solar wind characteristics averaged over 1 hour. For northward IMF, the correlation is fair on both sides, while for southward IMF, the correlation is negative and fairly low on the dayside (r = -0.18) but high on the nightside (-0.43). For the dynamic pressure, the correlation coefficients are high and are slightly higher on the nightside than on the dayside. In the light of these results, one would suspect that the solar wind kinetic energy flux $^{NV3}/_{2}$ (or $^{PV}/2$) would influence the proton precipitation processes. The correlation coefficients of the solar wind kinetic energy flux with the proton auroral precipitation are 0.50 and 0.46, respectively, for nightside and dayside aurora. The same calculation was made with the IMF magnetic energy flux, $^{(VB2)}/8\pi$. Correlation coefficients are slightly less than for the kinetic energy flux: 0.39 and 0.42 on nightside and on dayside, respectively.

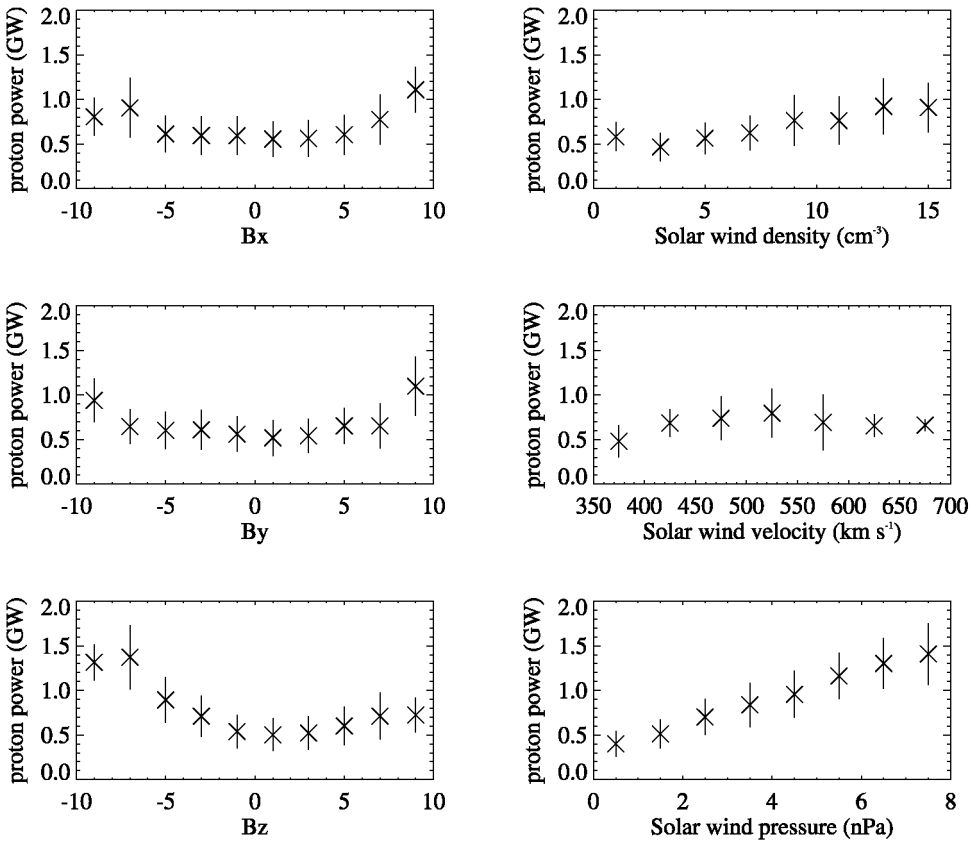

Figure 3. *Precipitated proton power versus IMF and SW characteristics on the nightside for both seasons. The power was averaged in SW ranges fixed in width. The proton power was evaluated in the sector between 2200 and 0200 MLT and between 60° and 80° MLAT. The left column panels show the dependence with the IMF orientation (B_x, B_y, and B_z), and the right panels are the dependence with the solar wind density, velocity, and dynamic pressure, respectively.*

[19] It was also shown that the nightside proton power increases for extreme values of positive and negative B_x. This influence of B_x is a priori difficult to understand as this component has no influence on the reconnection process nor on the magnetosphere stretching. However, we have shown in section 2 that the B_x component is fairly strongly correlated with B_y ($r = -0.50/-0.43$ for $B_z < 0/B_z > 0$) owing to the solar wind "garden hose" configuration. Moreover, values of $B_x < -6$ nT are strongly correlated with the solar wind velocity ($r = -0.83$) and fairly highly with the B_y component of the IMF ($r = 0.54$). The values of $B_x > 6$ nT are weakly correlated with B_y ($r = -0.25$), and moderately with the solar wind density ($r = 0.35$) and dynamic pressure ($r = 0.40$). These correlations probably explain the apparent influence of extreme B_x values on the proton and the electron power.

3.1. Solar Wind Dynamic Pressure Control

[20] The apparent linearity and the strong correlation found with the solar wind dynamic pressure suggest to analyze this relation in more detail. Figure 5 shows the slope of the linear regression between these two quantities in each 2-hour MLT sector. The regression was calculated separately by season and orientation of B_z, as it is known that these two parameters have an effect on the proton power [*Coumans et al.,* 2004b]. The slope was determined for proton power between 60° and 80° MLAT in all MLT sectors. The error bars plotted in the panel show the confidence interval of the linear regression. Figure 5 shows that the linear fit slope is globally higher in summer than in winter whatever the sign of B_z. This implies that the dynamic pressure influence is more active in summer. In both seasons, the regression slope is highest for southward IMF conditions on nightside. We note a local time dependence of the slope: a limited slope in the morning sector and a steeper slope over the dusk and the midnight sectors, indicating that the power increase with the dynamic pressure is largest in the night and dusk sectors. For all cases, a local minimum in the slope is observed in the evening sector. The lower slope values in this sector stem from the lower value of the proton power in the dynamic pressure range between 7 and 8 nPa. In this domain, the number of observations is substantially less than in the other bins. The

error bars in this sector are thus larger, at least in winter.

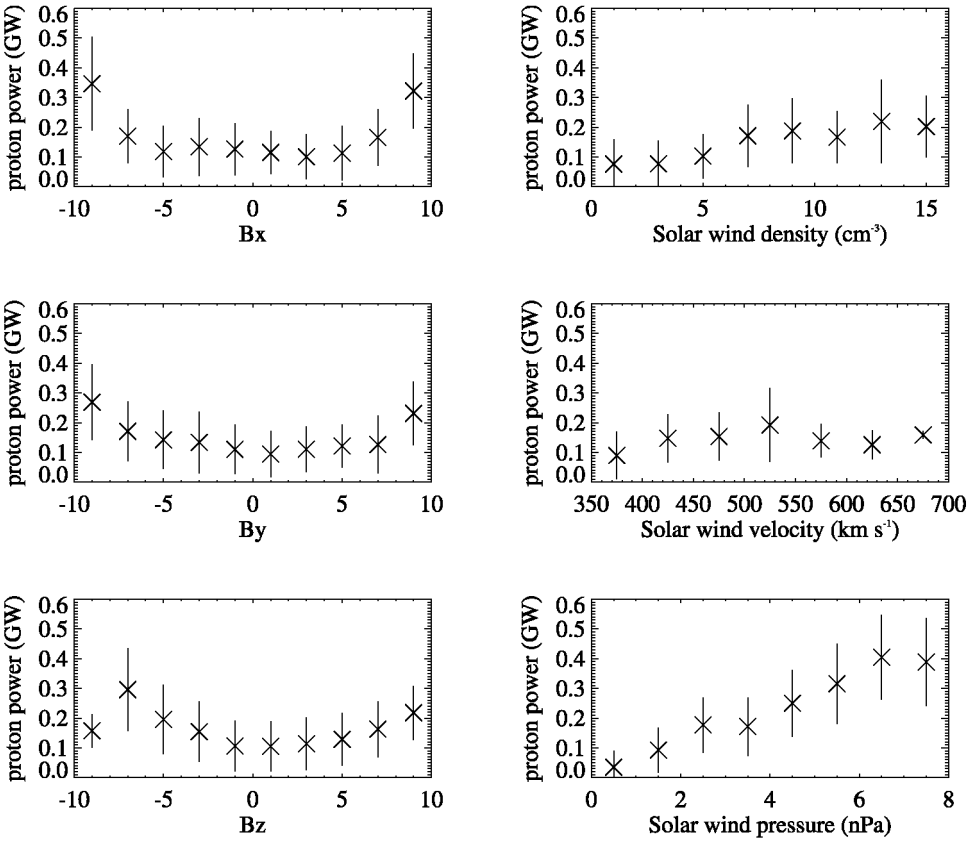

Figure 4. *Precipitated proton power versus IMF and SW characteristics on the dayside for both seasons. The power was averaged in SW ranges fixed in width. The proton power was evaluated in the sector between 1000 and 1400 MLT and between 60° and 80° MLAT. The left column panels show the dependence with the IMF orientation (B_x, B_y, and B_z), and the right panels are the dependence with the solar wind density, velocity, and dynamic pressure, respectively.*

3.2. Solar Wind-Magnetosphere Coupling

[21] We now analyze the energy coupling relation between the solar wind and the magnetosphere to understand how the interaction between them controls the proton precipitation. A list of coupling functions was summarized by *Liou et al.* [1998] together with their physical interpretation. Such empirical solar wind-magnetosphere energy coupling functions have been used as proxies of the energy input into the magnetosphere. Table 4 summarizes the correlation coefficient between the proton power and the value of the coupling function. B_t is the transverse component of the IMF and is equal to $\sqrt{B_y^2 + B_z^2}$; θ_c is the clock angle, i.e., the angle of the component of B in the Y-Z plane given by $\theta_c = \arccos(B_z/B_T)$. The correlations were calculated over the full database, for the nightside. The highest correlations are for $P^{1/3}\, VB^2{}_t \sin^4(\theta_c/2)$ [*Vasyliunas et al.,* 1982] and $P^{1/6}\, VB_t \sin^4(\theta_c/2)$ [*Vasyliunas et al.,* 1982], but large values are also found with $VB_t \sin(\theta_c/2)$ [*Gonzalez and Mozer,* 1974] and $VB_t \sin^2(\theta_c/2)$ [*Kan and Lee,* 1979]. The first two functions assume that the amount of energy which is transferred from the solar wind to the magnetosphere is proportional to the amount of solar wind kinetic energy intercepted by an energy gcollectionh region on the magnetopause [*Vasyliunas et al.,* 1982]. The two others involve the magneto spheric electric field in the Y-Z plane.

***Table 3**. Correlation Coefficients Between the Proton Power and the IMF North-South Component and the Solar Wind Dynamic Pressure for Nightside (Between 2200 and 0200 MLT) and Dayside (Between 1000 and 1400 MLT)*

	Nightside	**Dayside**
$B_z>0$	0.147 ±0.006	0.141 ± 0.006
$B_z<0$	-0.430 ± 0.005	-0.178 ± 0.006
P	0.483 ± 0.004	0.435 ± 0.005

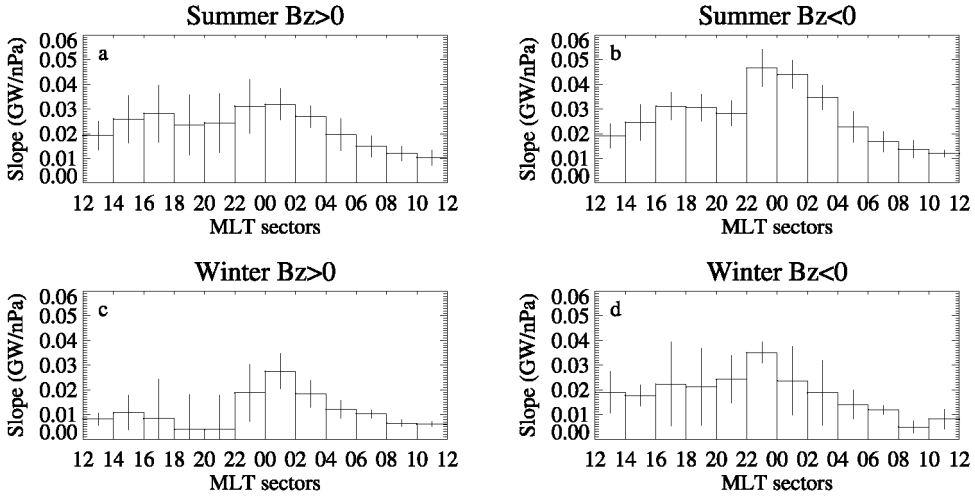

***Figure 5.** Slope (GW/nPa) of the linear regression between the proton power and the solar wind dynamic pressure, in summer (upper panels) and in winter (lower panels), for northward IMF (left panels) and for southward IMF (right panels). The slope was evaluated with the proton power separately in each 2-hours MLT sector.*

3.3. Solar Wind Data Delay

[22] As mentioned in section 1, the solar wind measurements from ACE satellite were first delayed by the propagation time between the satellite and the Earth using the velocity measurement. They were subsequently averaged over 1 hour before the IMAGE observation to consider the magnetosphere as a loading system. This 1-hour averaging was selected following a correlation analysis between the proton power and B_z. For their study of the solar wind control of the electron auroral precipitation, *Liou et al* [1998] used solar wind data delayed by 1 hour. As a check, we calculated correlations between proton power on nightside and solar wind data or coupling functions separately with solar wind data averaged over 1 hour and delayed by 1 hour. The correlation coefficients for hourly averaged solar wind characteristics are higher or, at the most, 1% lower (except for B_z > 0, where the difference is ~35%). In the case of the coupling functions, the correlation coefficients are also larger, except for VB^2_Z, where the difference is about 20% but the coefficient is moderate (0.30/0.25). Figure 6 shows the 2200-0200 MLT nightside proton power versus dynamic pressure for three different treatments: the triangles show the 1-hour average dynamic pressure dependence, the diamonds show the 1-hour delayed pressure, and the crosses show the instantaneous pressure (in fact, 1-min averaged). The error bars shows the statistical scatter of the powers by one standard deviation, for the 1-hour averaged dynamic pressure. The scatter is not shown for the other delayed pressures for clarity of the figure. The standard deviation is of the same order of magnitude for the other points. Figure 6 shows that the choice is not critical for dynamic pressure bins up to 5-6 nPa. Using the instantaneous, or 1-hour delayed, or 1-hour averaged dynamic pressure yields similar results. In the 6-7 nPa bin, the difference is less than 10% and about 30% in the 7+ nPa bin. The small difference between the results for the three delay times probably stems from the low statistical probability of high dynamic pressure events. Thus the probability for a same order of magnitude pressure 1 hour later or for the 1 -hour averaging is high. The behavior for the three delay times is thus quite similar, except for high dynamic pressures where the differences are maximum.

4. Fractional Electron and Proton Power

[23] The IMAGE-FUV instruments allow the study of the electron and proton auroral precipitation globally, simultaneously, and distinctly. It is thus possible to compare the simultaneous reaction of the precipitation of the two types of particles with changes in the solar wind and determine if this dependence is similar for both particles.

[24] First, a study of the solar wind control of the nightside and winter electron precipitation power, made in parallel of the proton precipitation one, has shown that the strongest correlations are for the north-south component of the IMF and for the solar wind velocity. The behavior of the electron power with B_z is nearly linear. The power is maximum for large negative B_z and decreases with increasing B_z. The orientation of B_z exerts the main control on the nightside precipitating electron power. Moreover, the power slowly increases with the velocity, but the scatter is high. The analysis of the coupling function response of the nightside electron power has shown that the strongest correlation is found for $P^{1/6}VB_T\sin^4(\theta_c/2)$ [*Vasyliunas et al.,* 1982] and $VB_T\sin^4(\theta_c/2)$ [*Wygant et al.,* 1983]. These two functions were also found by *Liou et al.* [1998] to be best correlated with the auroral brightness.

[25] The ratio between the proton and the electron power was evaluated and averaged over solar wind density, velocity and dynamic pressure ranges. Figure 7 shows the binned ratio as a function of the solar wind characteristics in winter, on nightside (between 2200 and 0200 MLT) and separately for positive and negative B_z. A ratio increase implies that the proton power increases more than the electron power with the solar wind parameters. Results show that the proton power is more dependent on the solar wind density than the electron power, whatever the sign of B_z. The regression slope values are quite close (within 10%). The velocity control of the particle precipitation shows a negative slope, for both signs of B_z, meaning that electrons are more reactive to variations of the velocity than protons. For negative B_z, the slope is lower than for positive B_z. In fact, the regression slopes for both particles separately are lower for negative B_z than for positive B_z. Finally, the most contrasted result is for dynamic pressure. The slope of the regression is much higher for positive B_z than for negative B_z. Moreover, the slope is close to zero for southward IMF. These results show that the protons are more influenced by a dynamic pressure increase than the electrons when B_z is positive while the effect is similar for both particles for negative B_z values.

Table 4. *Correlation Coefficient Between Proton Power and 11 Coupling Functions on Nightside*[a]

	Nightside
VB_Z	-0.210 ± 0.005
VB_t	0.417 ± 0.005
V^2B_Z	-0.225 ± 0.005
VB_Z^2	0.246 ± 0.005
$VB_t \sin(\theta_c/2)$	0.465 ± 0.005
$VB_t \sin^2(\theta_c/2)$	0.457 ± 0.005
$VB_t \sin^4(\theta_c/2)$	0.434 ± 0.005
$VB^2 \sin^4(\theta_c/2)$	0.397 ± 0.005
$P^{1/2}VB_Z$	-0.187 ±0.006
$P^{1/3}\ VB_t^2 \sin^4(\theta_c/2)$	0.486 ± 0.004
$P^{1/6}\ VB_t \sin^4(\theta_c/2)$	0.477 ± 0.005

[a] *The solar wind characteristics were averaged over 60 min before the IMGE-FUV snapshot.*

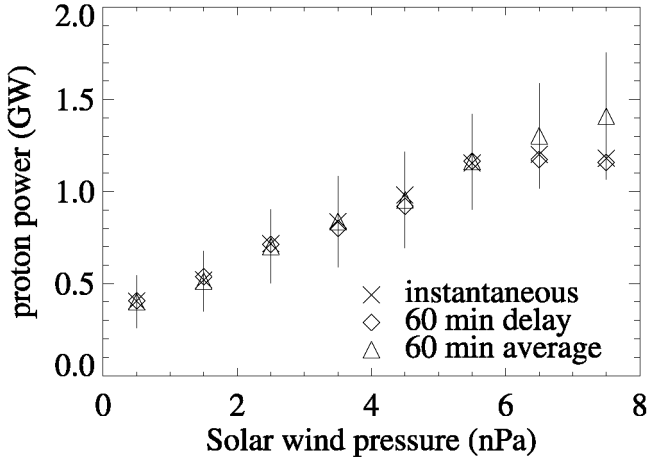

Figure 6. *Precipitated proton power versus the solar wind dynamic pressure for three different delay times. The triangles show the 1-hour average dynamic pressure dependence, the diamonds show the 1-hour delayed pressure, and the crosses show the instantaneous pressure (in fact, 1-min averaged). The error bars show the statistical 1-σ scatter of the power, for the 1-hour averaged dynamic pressure. The standard deviation for the other two cases (not shown for clarity) is on the same order of magnitude.*

[26] Finally, we investigate the slope of the regression between the proton and the electron power. Figure 8 shows the slope evolution as a function of the Kp index. A regression was calculated between the proton and the electron powers in the night sectors, over the full range of data, separately for each range of Kp values. A high slope value implies that the precipitating proton flux is proportionally larger compared to the electron flux when the total auroral flux increases. A nearly null slope shows that the proton proportion in the total flux is similar when the flux increases. Figure 11 shows that the slope is higher for Kp < 4. This result was expected since, for low activity, the proton contribution in the total flux is higher, for example before substorms [*Hubert et al.,* 2002; *Coumans et al.,* 2004a]. The black column for Kp = 5 corresponds to the absence of data for this Kp value.

5. Discussion

5.1. Proton Precipitation Processes

[27] As described earlier, one of the mechanisms of nightside proton precipitation is linked to the magnetic field line stretching in the magnetotail. The ions traveling through the magnetotail magnetic field reversal are submitted to scattering of their magnetic moment, which can be viewed as an impulsive centrifugal force perturbing the particle gyromotion [*Delcourt et al.,* 1996]. As a result of magnetic damping in the field reversal, the loss cone can be filled. This stochastic pitch angle distribution appears when the magnitude of the centrifugal force is on the order of the Lorentz force of the magnetic field. This condition is especially fulfilled in regions where the magnetic field varies significantly within a cyclotron radius, in the near-Earth tail, and forms an associated sharp transition from dipole-like to tail-like magnetic field. For weakly curved field lines (dipole approximation), the ion motion in the magnetic field is adiabatic (with the conservation of the magnetic moment as a first-order invariant of motion). When the curvature is on the order of magnitude of the gyromotion radius, chaos becomes strong, leading to the injection of the ions into the loss cone, hence their precipitation into the ionosphere. *Sergeev et al.* [1983] found from magneto spheric magnetic field model simulations that the stochastization process of protons is limited for stretched field lines where $R_c/\rho > 8$, where R_c is the field line curvature radius at the equator and ρ is the Larmor gyrora-dius. Since this stochastic precipitation takes place in the absence of wave-particle interactions, it occurs even during very quiet geomagnetic conditions. A change in the shape of the magnetosphere, e.g., due to a change in the solar wind conditions, will modify the source region of the precipitating ions. An increase in the dynamic pressure produces a modification of the topology of the magnetosphere, compressing the field lines of the dayside magnetosphere and stretching the field lines on the opposite side, leading to variations of the intensity of the precipitation proton flux on the nightside [*Tsyganenko,* 1990]. Particles that were trapped on dipolar field lines are now on stretched field lines and can precipitate into the ionosphere. Thus variations of the amount of stretching affect of the nightside proton precipitation characteristics with the dynamic pressure variations.

[28] The mechanisms causing proton precipitation on the dayside are different from the nightside. A modification in the dynamic pressure and in the compression level of the dayside field lines was shown to influence proton precipitation. On the dayside, the dependence of the proton power on the dynamic pressure is not as high as on the nightside. The less pronounced effect on the dayside supports the idea that the mechanisms are different from the nightside. The dayside auroral precipitation originates from different plasma sources, which can be of solar wind/magnetosheath or of inner magnetosphere origin. The dayside cusp is the area where magnetosheath plasma can most easily access the ionosphere. Statistical studies confirmed the localized nature of the cusp near local noon *[Newell and Meng,* 1994]. However, magnetosheath protons that precipitate in the cusp have typical energies of ~1 keV. The FUV-SI12 camera is mostly sensitive to precipitating protons with initial energies of 2-8 keV [*Gérard et al.,* 2000]. Consequently, only energetic protons observed during periods of enhanced solar wind dynamic pressure produce emissions measured by SI12 [*Fuselier et al.,* 2001]. Observability of cusp proton precipitation by SI12 is thus expected to be strongly influenced by variations of dynamic pressure. Consequently in this statistical study, cusp precipitation is not the main component on the dayside over the time period we analyzed. Other mechanisms for dayside proton precipitation have been proposed by *Sergeev et al.* [1997]. They showed, using magneto spheric models, that a weak magnetic field in the outer cusp inevitably contributes to regular scattering of energetic protons on closed field lines in a ~2-3 hour wide MLT sector centered on noon. They also emphasized a second zone of dayside proton precipitation, formed by scattering on closed field lines crossing the nightside equatorial region near the magnetopause. Such field lines have their footprint in the dayside sector and are curled toward the nightside where they cross the equatorial plane. This mechanism provides isotropic precipitation in a sector located ~1.5-2 hours MLT from noon, which smoothly connects with the precipitation originating from the tail current sheet. Their model computations showed that, moving away from noon in magnetic local time, the outermost closed field line remain approximately in the meridian plane until they reach the outer cusp latitude, where they sharply turn tailward and cross the equatorial region near the magnetopause. Central plasmasheet protons injected in the night sector, which subsequently drift to the dayside also contribute to proton dayside precipitation. Finally, proton precipitation on the dayside may also be caused by plasma turbulence [*Sergeev et al.,* 1997, *Clemmons et al.,* 2000].

5.2. Role of Solar Wind Dynamic Pressure

[29] We previously discussed how solar pressure controls the nightside proton precipitation through the stretched magnetotail. Our results suggest that compression due to a dynamic pressure increase also influence proton precipitation on the dayside. It is likely that the shape of the closed field lines crossing the nightside equatorial region near the magnetopause [*Sergeev et al.,* 1997] is not so stretched as the tail ones when the dynamic pressure increases. But other mechanisms also operate. The dynamic pressure plays an important role for aurora generated by a sudden increase of dynamic pressure. Fast and high dynamic pressure jumps generate Alfvén waves and pitch angle scattering inducing dayside auroral enhancements, respectively, at high and low latitudes. The role of these mechanisms was confirmed by in situ measurements [*Zhou et al.,* 2003; *Meurant et al.,* 2003b]. In addition to the above processes, strong compressions of the magnetopause and the outer magnetosphere also lead to particle precipitation due to lowering of the mirror points of trapped particles to altitudes below 100 km [*Spann et al.,* 1998]. Adiabatic compression leads to loss cone instability, wave growth, and enhanced pitch angle scattering [*Zhou and Tsurutani,* 1999; *Tsurutani et al.,* 2001]. These mechanisms may also be present for high dynamic pressure not resulting from shocks.

[30] Complementary analysis shows that the increase in the power with P_{dyn} is due to an increase of the latitudinal width of the precipitation region and to an enhanced brightness of the proton aurora. For different classes of solar wind dynamic pressures, we calculated maps of the average precipitating proton flux. The result was that the power increase is due to both a widening and an intensification of the proton auroral region. The question is then whether field line stretching can be the cause of both types of increase. It is easy to explain the widening of the precipitation region. If the magnetotail is more stretched, more magnetic field lines fulfill the criterion of the proton scattering. The stochastization area becomes larger, extending closer to the Earth, and the footprints of these field lines spread over a larger ionospheric region. Stretching of the magnetotail may also influence the brightness of the proton emission and thus the intensity of precipitating flux. The field lines which are more stretched following an increase of the solar wind dynamic pressure cross the equatorial plane of the magnetotail in a region different than before the increase of stretching. If the plasma sheet density of this region is higher or if the plasma is hotter, the proton precipitating flux would increase. This plasma sheet proton density or temperature change may be either intrinsic to the plasmasheet distribution or due to a simultaneous increase of the density or variation of the temperature caused by new plasma injection for example. This second explanation would imply that more complex dynamical processes than a simple increase of the stretching take place in the magnetosphere, involving the transfer from the solar wind to the magnetosphere and the transfer to the tail. The

correlation coefficients are larger using coupling functions than for solar wind parameters alone. This result is one additional clue suggesting that a number of different mechanisms control particle precipitation. Auroral precipitation is not the effect of one isolated change in the solar wind dynamic pressure or in the velocity. A collection of parameters acts together to control particle precipitation and the aurora. The fact that the correlation coefficients are globally quite low, always below 0.55, is another piece of evidence showing the multiplicity of the processes controlling the particle precipitation.

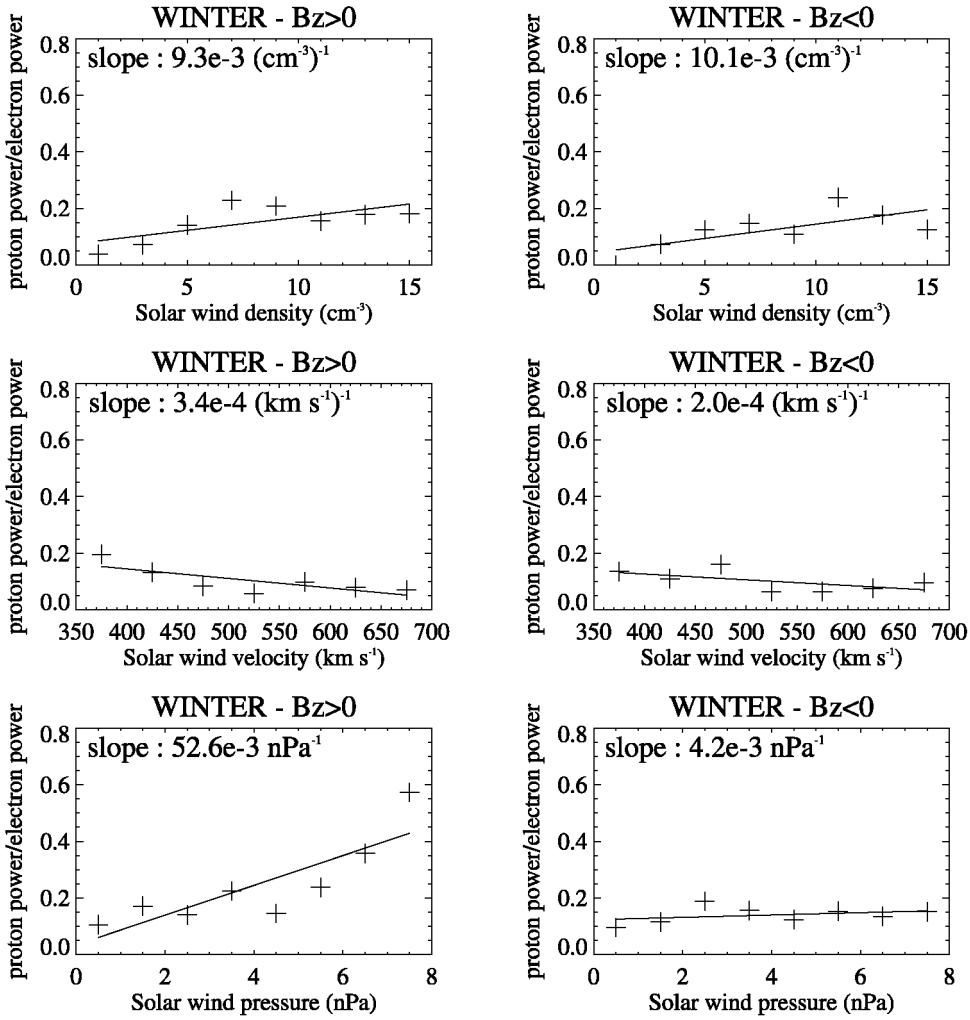

Figure 7. *Variation of the ratio of proton to the electron powers with the solar wind density (upper panels), velocity (medium panels) and dynamic pressure (lower panels). The ratios were calculated in winter, on the nightside (between 2200 and 0200 MLT) and separately for positive B_z (left panels) and negative B_z (right panels). A linear fit is added and the slope is indicated for each case.*

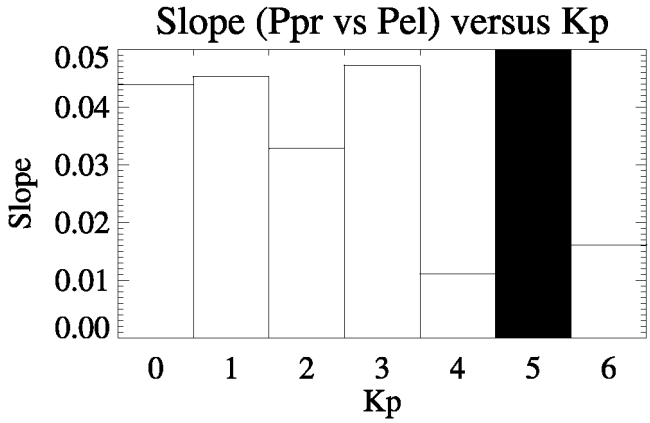

Figure 8. *Slope of the linear regression between the proton and the electron power as a function of the Kp ranges. The powers were evaluated in the night sector (2200-0200 MLT), with winter data. No data are available for Kp = 5.*

5.3. Solar Wind-Magnetosphere Coupling

[31] Reconnection between the IMF and the magneto-spheric field lines also plays a role on proton precipitation. Our results have shown that the dynamic pressure has more influence on the proton precipitation for southward IMF than for northward IMF, especially on the nightside. It is established that reconnection takes place at the front of the magnetopause for antiparallel configuration, i.e., for southward IMF, while the merging region is located at higher latitude for northward IMF. The antiparallel reconnection induces a large fresh plasma injection from the solar wind to the magnetosphere. This plasma reaches the plasma sheet through magneto spheric convection. The dynamic pressure control on the tail stretching is then more efficient since more plasma is preconditioned to be accelerated. It is possible that the different dependence of the proton power on the dynamic pressure according to the IMF north-south orientation is due to an influence of the dynamic pressure on the reconnection efficiency. It was shown in section 2 and Table 2 that the correlation between the dynamic pressure and the intensity of B_z according its sign was weak but stronger for $B_z > 0.1$. The effects on the reconnection efficiency of the orientation of the B_z component and the pressure intensity may be coupled.

[32] Our coupling function study shows that the proton power mostly responds to the solar wind kinetic energy that is intercepted by the magnetopause. This kinetic energy depends on the dynamic pressure which controls the magnetotail stretching as described above. The correlation with the coupling function in this case may not be characteristic of the energy transferred from the solar wind to the magnetosphere via the magnetopause. The influence could also result from the modification of the magnetospheric shape due to changes in the solar wind kinetic energy. The stretching rate of the magnetosphere may be dependent of the energy transfer between the solar wind and the magnetosphere. However, magnetospheric stretching is probably the main cause of proton nightside precipitation during quiet activity level. In this case, the solar wind influence on the auroral proton precipitation is indirect and mainly due to the solar wind control of the magnetospheric shape.

5.4. Response of Electrons and Protons to Solar Wind Characteristics

[33] Our study of the ratio of the nightside proton and electron simultaneous precipitation showed that the regression slope is lower for high Kp values, meaning that for high activity level, the proportion of the proton power remains unchanged when total auroral power increases. For low activity levels, the precipitating proton flux proportionally increases in relation to the electron flux. The similar behavior of protons and electrons for high activity levels may be a consequence of identical mechanisms of energization for both types of particles, especially during sub-storms. Fresh plasma is injected from the solar wind to the plasma sheet by reconnection mechanisms. During quiet activity periods, the precipitation mechanisms are probably different and bear different signatures of the solar wind influence. As explained before, during quiet periods, proton aurora is dominated by chaotization of the proton distribution on the stretched field line, a mechanism which is not efficient for electrons. By contrast, during active periods, precipitation of both particles is due to new plasma injection into the plasma sheet or to a compressed magnetic reconfiguration. In this last case, particles which were stably trapped are precipitated following compression of the mag-netosphere and reconfiguration of the shape of the guiding lines.

[34] In addition, we have also shown that an increase in the solar wind density increases the proton power proportion in the total auroral precipitation while an increase in the solar wind velocity increases the electron proportion, whatever the B_z orientation. Morevover, the nightside protons are more influenced by a dynamic pressure increase than electrons when B_z is positive while the effect is similar for both types of particles for negative B_z. This last result reinforces the above-described mechanisms, since a southward IMF orientation is favorable to substorm development. The precipitation mechanisms are similar and the effect of the dynamic pressure is then attenuated. For northward IMF, the protons are more influenced by the dynamic pressure controlling the levels of magneto spheric stretching and the efficiency of proton precipitation via the chaotization mechanism in the magnetotail.

6. Summary

[35] The main result of the correlation study between the proton auroral power and the solar wind characteristics is that the power of the precipitated protons is mainly controlled by the solar wind dynamic pressure, at least during periods of solar activity maximum. The main cause of this control on the nightside appears related to dynamic pressure effect on the shape of the magnetosphere and thus the amount of magnetotail stretching. On the dayside, the dynamic pressure also plays a role, although the precipitation mechanisms are different from those on the nighside. We have shown that the magnitude of the southward IMF component has more control on the nightside proton power than on the dayside. Moreover, the orientation of the IMF has an influence on the dynamic pressure effect mainly on the nightside power. These results confirm the multiplicity of the processes controlling auroral proton precipitation.

[36] The correlation is higher between the nightside proton power and the coupling functions $P^{1/3}\ VB^2_t \sin^4(\theta_c/2)$ and $P^{1/6}\ VB_t \sin^4(\theta_c/2)$ [*Vasyliunas et al.,* 1982] than with other proposed solar wind coupling formulae. These assume that the amount of energy transferred from the solar wind to the magnetosphere is proportional to the solar wind kinetic energy intercepted by the magnetopause. The presence of the dynamic pressure factor in these functions suggests that the changes in the solar wind kinetic energy exerts some control on the shape of the magnetotail and thus on the proton stochastization process. We have also shown that significant correlations are found with $VB_t \sin(\theta_c/2)$ [*Gonzalez and Mozer,* 1974] and $VB_t \sin^2(\theta_c/2)$ [*Kan and Lee,* 1979], two alternative proxies for the magnetospheric electric field in the Y-Z plane.

[37] Results described above were obtained with 1-hour averaged solar wind data, which precludes analysis of short-term correlations. Nevertheless, we also showed that correlations between proton power and instantaneous, 1-hour averaged or 1-hour delayed dynamic pressure yields very similar results. This indicates that the choice of the averaging time is not critical, a result explained by the rather rare occurrence of high dynamic pressure events.

Acknowledgments.

VC is supported by a fellowship from the Belgian Fund for Research in Industry and Agriculture (FRIA) and JCG and BH are supported by the Belgian National Fund for Scientific Research (FNRS). This work was funded by the PRODEX program of the European Space Agency (ESA) and the Belgian Fund for Collective and Fundamental Research (FRFC grant 2.4517.02). The authors thank to S. W. H. Cowley and B. Emery for valuable comments on the manuscript.

References

Akasofu, S.-I. (1981), Energy coupling between the solar wind and the magnetosphere, *Space Sci. Rev., 28,* 121.

Arnoldy, R. L. (1971), Signature in the interplanetary medium for substorms, *J. Geophys. Res*., *76*, 5189.

Chua, D., G. Parks, M. Brittnacher, W. Peria, G. Germany, J. Spann, and C. Carlson (2001), Energy characteristics of auroral electron precipitation: A comparison of substorms and pressure pulse related auroral activity, *J. Geophys. Res*., *106*, 5945.

Clemmons, J. H., et al. (2000), Observations of traveling Pc5 waves and their relation to the magnetic cloud event of January 1997,

J. Geophys. Res., *105*, 5441.

Coumans, V., J.-C. Gérard, B. Hubert, and D. S. Evans (2002a), Electron and proton excitation of the FUV aurora: Simultaneous IMAGE and NOAA observations, *J. Geophys. Res*., *107*(A11)*,* 1347.

Coumans, V., J.-C. Gérard, B. Hubert, M. Meurant, and S. B. Mende (2004), Global auroral conductance distribution due to electron and proton precipitation from IMAGE-FUV observations, *Ann. Geophys*., *22*, 1595.

Coumans, V., J.-C. Gérard, B. Hubert, S. B. Mende, and S. W. H. Cowley (2004b), Morphology and seasonal variations of global auroral proton precipitation observed by IMAGE-FUV, *J. Geophys. Res*., *109*, A12205.

Delcourt, D. C, J.-A. Sauvaud, R. F. Martin Jr., and T. E. Moore (1996), On the nonadiabatic precipitation of ions from the near-Earth plasma sheet, *J. Geophys. Res*., *101*, 17,409.

Frey, H. U., S. B. Mende, T J. Immel, S. A. Fuselier, E. S. Claflin, J.-C Gérard, and B. Hubert (2002), Proton aurora in the cusp, *J. Geophys. Res*., *107*(A7)*,* 1091.

Fuselier, S. A., et al. (2001), Ion outflow observed by IMAGE: Implications for source regions and heating mechanisms, *Geophys. Res. Lett*., *28*, 1163.

Gérard, J.-C., B. Hubert, D. V. Bisikalo, and V. I. Shematovich (2000), A model of Lyman-α line profile in the proton aurora, *J. Geophys. Res*., *105*, 795.

Gonzales, W. D., and F. S. Mozer (1974), A quantitative model for the potential resulting from reconnection with an arbitrary interplanetary magnetic field, *J. Geophys. Re*s., *79*, 4186.

Hardy, D. A., M. S. Gussenhoven, and D. Brautigam (1989), A statistical model of auroral ion precipitation, *J. Geophys. Res*., *94*, 370.

Hardy, D. A., W. McNeil, M. S. Gussenhoven, and D. Brautigam (1991), A statistical model of auroral ion precipitation: 2. Functional representation of the average patterns, *J. Geophys. Res*., *96*, 5539.

Hubert, B., J. C. Gérard, D. S. Evans, M. Meurant, S. B. Mende, H. U. Frey, and T. J. Immel (2002), Total electron and proton energy input during auroral substorms: Remote sensing with IMAGE-FUV, *J. Geophys. Res*., *1*07(A8), 1183.

Hubert, B., J-C. Gérard, A. Fuselier, and S. B. Mende (2003), Observation of dayside subauroral proton flashes with the IMAGE-FUV imagers, *Geophys. Res. Lett*, 30(3), 1145.

Jacobsen, B., P. E. Sandholt, W. J. Burke, W. F. Denig, and N. C. Maynard (1995), Optical signatures of the prenoon auroral precipitation: Sources and responses to solar wind variations, *J. Geophys. Res*., *100*, 8003.

Kamide, Y., and J. D. Winningham (1977), A statistical study of the "instantaneous" nightside auroral oval: The equatorward boundary of the electron precipitation as observed by the Isis 1 and 2 satellites, *J. Geophys. Res*., *82*, 5573.

Kan, J. R., and L. C. Lee (1979), Energy coupling functions and solar wind magneto sphere dynamo, *Geophys. Res. Lett*., *6*, 577.

Lasen, K., and C. Danielsen (1978), Quiet time pattern of auroral arcs for different directions of the interplanetary magnetic field in the Y-Z plane, *J. Geophys. Res*., *83*, 5277.

Liou, K., P. T. Newell, C.-I. Meng, M. Brittnacher, and G. Parks (1998), Characteristics of the solar wind controlled auroral emissions, *J. Geophys. Res*., *103*, 17,543.

Makita, K., C.-I. Meng, and S.-I. Akasofu (1983), The shift of the auroral electron precipitation boundaries in the dawn-dusk sector in the association with geomagnetic activity and interplanetary magnetic field, *J. Geophys. Res*., *88*, 7967.

Mende, S. B., et al. (2000), Far Ultraviolet imaging from the IMAGE spacecraft. 1. System design, *Space Sci. Rev*., *91*, 243.

Mende, S. B., H. U. Frey, T J. Immel, D. G Mitchell, and J. C. Gérard (2002), Global comparison of magneto spheric ion fluxes and auroral precipitation during a substorm, *Geophys. Res. Lett*., *29*(12), 1609.

Meurant, M., J.-C. Gérard, B. Hubert, V. Coumans, V. I. Shematovich, D. V. Bisikalo, D. S. Evans, G. R. Gladstone, and S. B. Mende (2003a), Characterization and dynamics of the auroral electron precipitation during substorms deduced from IMAGE-FUV, *J. Geophys. Res*., *108*(A6), 1247.

Meurant, M., J.-C. Gérard, B. Hubert, V. Coumans, C. Blockx, N. Østgaard, and S. B. Mende (2003b), Dynamics of global scale electron and proton precipitation induced by a solar wind pressure pulse, *Geophys. Res. Lett*., *30*(20), 2032.

Newell, P. T., and C.-I. Meng (1994), Ionospheric projections of magneospheric regions under low and high solar wind pressure conditions, *J. Geophys. Res*., *99*, 273.

Newell, P. T, S. Wing, T. Sotirelis, and C.-I. Meng (2005), Ion aurora and its seasonal variations, *J. Geophys. Res*., *110*, A01215, doi:10.1029/ 2004JA010743.

Perreault, P., and S.-I. Akasofu (1978), A study of geomagnetic storms, *Geophys. J.R. Astron. Soc*., *54*, 547.

Sergeev, V. A., E. M. Sazhina, N. A. Tsyganenko, J. Å. Lundblad, and F. Søraas (1983), Pitch-angle scattering of energetic protons in the mag-netotail current sheet as the dominant source of their isotropic precipitation into the nightside ionosphere, *Planet. Space Sci*., *31*, 1147.

Sergeev, V. A., G. R. Bikkuzina, and P. T. Newell (1997), Dayside isotropic precipitation of energetic protons, *Ann. Geophys*., *15*, 1233.

Shue, J.-H., P. T. Newell, K. Liou, and C.-I. Meng (2002), Solar wind density and velocity control of auroral brightness under normal interplanetary magnetic field conditions, *J. Geophys. Res*., *1*07(A12), 1428, doi:10.1029/2001JA009138.

Solomon, S. C., P. B. Hays, and V. Abreu (1988), The auroral 6300 Å emission: Observation and modeling, *J. Geophys. Res*., *93*, 9867.

Spann, J. F., M. Brittnacher, R. Elsen, G. A. Germany, and G. K. Parks (1998), Initial response and complex polar cap structures of the aurora in response to the January 10, 1997 magnetic cloud, *Geophys. Res. Lett*., *25*, 2577.

Tsurutani, B. T., et al. (2001), Auroral zone dayside precipitation during magnetic storm initial phases, *J. Atmos. Sol. Terr. Phys*., *63*, 513.

Tsyganenko, N. A. (1990), Quantitative models of the magneto spheric magnetic field: Methods and results, *Space Sci. Rev*., *54*, 75.

Vasyliunas, V. M., J. R. Kan, G. L. Siscoe, and S.-I. Akasofu (1982), Scaling relations governing magnetospheric energy transfer, *Planet. Space Sci*., *30*, 359.

Wygant, J. R., R. B. Torbert, and F. S. Mozer (1983), Comparison of the S3-3 polar cap potential drops with the interplanetary magnetic field and models of magnetopause reconnection, *J. Geophys. Res*., *88*, 5727.

Zhou, X., and B. T. Tsurutani (1999), Rapid intensification and propagation of the dayside aurora: Large scale interplanetary pressure pulses (fast shocks), *Geophys. Res. Lett*., *26*, 1097.

Zhou, X.-Y, R. J. Strangeway, P. C. Anderson, D. G. Sibeck, B. T. Tsurutani, G. Haerendel, H. U. Frey, and J. K. Arballo (2003), Shock aurora: FAST and DMSP observations, *J. Geophys. Res*., *108*(A4), 8019.